electronic reprint

Journal of
Applied Crystallography
ISSN 0021-8898
Editor: **Gernot Kostorz**

Tracking reflections through cryogenic cooling with topography

Jeffrey J. Lovelace, Cameron R. Murphy, Reinhard Pahl, Keith Brister and Gloria E. O. Borgstahl

Journal of
Applied Crystallography
ISSN 0021-8898

Received 22 November 2005
Accepted 7 April 2006

Tracking reflections through cryogenic cooling with topography

Jeffrey J. Lovelace,[a] Cameron R. Murphy,[a] Reinhard Pahl,[b] Keith Brister[b,c] and Gloria E. O. Borgstahl[a]*

[a]Eppley Institute for Research in Cancer and Allied Diseases, 987696 Nebraska Medical Center, Omaha, NE 68198-7696, USA, [b]BioCARS - The University of Chicago, 9700 South Cass Ave. Bldg. 434B, Argonne, IL 60439, USA, and [c]LS-CAT, Northwestern University, 9700 South Cass Av., Bldg. 436A, Argonne, IL 61439, USA. Correspondence e-mail: gborgstahl@unmc.edu

The mosaic structure of a single protein crystal was analyzed by reflection profiling and topography using highly parallel and monochromatic synchrotron radiation. Fine-φ-sliced diffraction images (0.002° stills) were collected using a conventional large-area CCD detector in order to calculate reflection profiles. Fine-φ-sliced topographic data (0.002°) stills were collected with a digital topography system for three reflections in a region where the Lorentz effect was minimized. At room temperature, several different mosaic domains were clearly visible within the crystal. Without altering the crystal orientation, the crystal was cryogenically frozen (cryocooled) and the experiment was repeated for the same three reflections. Topographs at cryogenic temperatures reveal a significantly increased mosaicity, while the original domain structure is maintained. A model for the observed changes during cryocooling is presented.

1. Introduction

X-rays damage protein crystals. To prolong the useful life of samples for protein crystallography, especially with synchrotron radiation, the crystals are typically cryocooled during the data collection. Although cryocooling does greatly increase the life span of the crystal, it basically always increases the rocking widths of the reflections, possibly even causing deformation and/or splitting of the reflection profiles. Mosaic crystals were first conceptualized by Darwin (1922) as being made up of essentially perfect crystal domains that are slightly misaligned with respect to one another. Since the domains are slightly misaligned, the domains enter diffraction conditions at slightly different angles, leading to complex observed reflection profiles that are a composite of those from the individual mosaic domains. Helliwell (1988) derived a theoretical limit for a perfect protein crystal, including very fine mosaicity measurements, and later extending the study to a sufficiently collimated synchrotron radiation X-ray beam to probe the intrinsic quality of insulin crystals as a test case (Colapietro *et al.*, 1992). Subsequently, others (Fourme *et al.*, 1995; Snell *et al.*, 1995; Nave, 1998; Boggon *et al.*, 2000; Vahedi-Faridi *et al.*, 2003; Borgstahl *et al.*, 2001; Bellamy *et al.*, 2000) undertook a variety of mosaicity, topography and reciprocal-space mapping experiments that examined protein crystal perfection. These studies revealed domains and values of intrinsic mosaicity very close to the theoretical limit. Furthermore, basically, the more the domains are misaligned, the bigger this contribution to the crystal's reflection profiles will be. Variations in the unit-cell dimensions within a mosaic domain will also cause a broadening of the reflection profile from the individual domains. It is an extra challenge to distinguish these two effects from the analysis of reflection profiles and mosaicity alone (Vahedi-Faridi *et al.*, 2003). Topography, in particular, provides a very effective complimentary technique that can directly image the mosaic domains to help study these various phenomena.

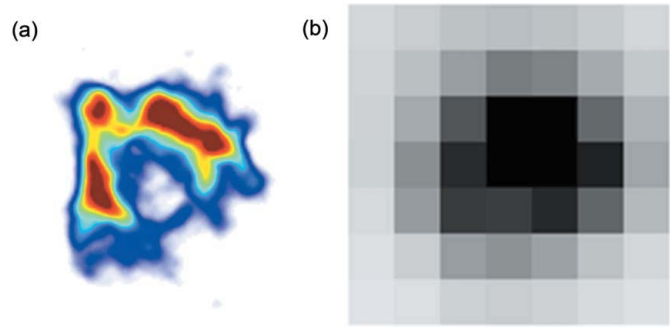

Figure 1
Effect of detector pixel resolution on single-crystal diffraction data. Data were collected with (*a*) a topography camera with a pixel size of 8 × 8 μm pixels, and (*b*) an ADSC Quantum-4 detector with 81.6 × 81.6 μm pixels.

Topographs are images of an individual reflection at high spatial resolution. Typically, topographic measurements are made with nuclear emulsions or other high-resolution film (Fourme *et al.*, 1995; Stojanoff & Siddons, 1996; Stojanoff *et al.*, 1997, 1996; Dobrianov *et al.*, 1998; Otálora *et al.*, 1999; Boggon *et al.*, 2000). Film methods have several experimental drawbacks that can be overcome by substituting the film for a CCD detector with a small pixel size (~8 μm) (Ludwig *et al.*, 2001;

Table 1
Data collection summary.

Run	Temperature	Detector	Starting φ	Width ($\Delta\varphi$)	Type	Images	Exposure time (s)	Scale factors†
1	RT	ADSC	0.000°	1.000°	Oscillation	5	10	0.924 (0.021)
2	RT	ADSC	1.800°	0.002°	Still	700	1	
3	RT	ADSC	0.000°	1.000°	Oscillation	5	10	1.054 (0.021)
4	RT	Topography	1.914°	0.002°	Still	250	4	
5	CR	Topography	1.414°	0.002°	Still	525	4	
6	CR	ADSC	0.000°	1.000°	Oscillation	5	10	
7	CR	ADSC	1.300°	0.002°	Still	650	2	

† Scale factors between images were calculated by integrating the ten coarse images ($\Delta\varphi = 1°$) with *MOSFLM* and scaling them together with *SCALA*. Average values for the five images in each run are given with standard deviations in parentheses.

Lovelace, Soares *et al.*, 2004; Lübbert *et al.*, 2004). Such high-resolution CCDs generally cover only a very small active area (∼8 × 8 mm) as compared with CCD-based area detectors (∼200 × 200 mm) commonly used in protein crystallography. In order to index the crystal as well as collect topographs, we use both the large-area detector and the topography CCD (Lovelace *et al.*, 2005). Fig. 1 shows a digital topograph compared with the same reflection captured by an ADSC Quantum-4 detector to illustrate the significant improvement in spatial information.

In this experiment, we collected topographic sequences for identical reflections with an identical crystal orientation under room temperature (RT) and cryogenic (CR) conditions. This was done to observe and quantify the effects of cryocooling on protein crystals with respect to the mosaic domain structure of the crystal. Special consideration was taken to minimize crystal slippage and maintain mechanical accuracy.

2. Experimental methods

2.1. Crystal preparation

Chicken egg-white lysozyme was obtained from Sigma (L-6876) and used without further purification. Tetragonal lysozyme crystals were mounted in capillaries and fixed with glue to reduce mechanical slippage (Fig. 2*a*) (Knapp *et al.*, 2004; Rayment *et al.*, 1977). Several types of glue were tried and epoxy glue was selected for lysozyme crystals. The capillary was securely fixed on a brass pin which was mounted on the goniometer head. For CR conditions, the cryogenic system was rapidly adjusted to a preset position, blowing the cold stream directly over the crystal location in the capillary (Yao *et al.*, 2004). These cryo methods were optimized at the home laboratory and were found to give cryocooled lysozyme diffraction data similar to conventional loop-based methods employing glycerol as the cryo-protectant (data unpublished but in essence involved comparative resolution-limit checks).

2.2. Overall experimental setup

BioCARS beamline 14-BM-D at the Advanced Photon Source (APS) was used in unfocused mode to minimize the beam divergence (Bellamy *et al.*, 2000). The vertical and horizontal beam divergences were determined to be 22 and 45–90 µrad, respectively, with $\Delta\lambda/\lambda = 4.00 \times 10^{-4}$. Two different types of diffraction experiments were performed. One was fine φ-slicing to measure many reflection profiles using an ADSC Quantum-4 detector. The other was the collection of single-reflection topographs using a high-resolution imaging CCD. The topography system was installed parasitically at the beamline as described previously (Lovelace *et al.*, 2005). This method has the benefit of allowing topographs to be collected with the existing beamline control software and collecting conventional data when the topography camera is stowed.

2.3. Overall data collection strategy

First, a series of coarse oscillation images were collected for the purposes of indexing and selecting a group of reflections located in the vertical sectors of the image such that the effects of beam divergence and the Lorentz effect were minimized. Reflections within an 8 × 8 mm area were selected with $\varsigma \simeq 0$ (*i.e.* the reciprocal-space coordinate parallel to the rotation axis of the crystal), chosen to minimize the Lorentz reflection-broadening effect (Greenhough & Helliwell, 1982) to match

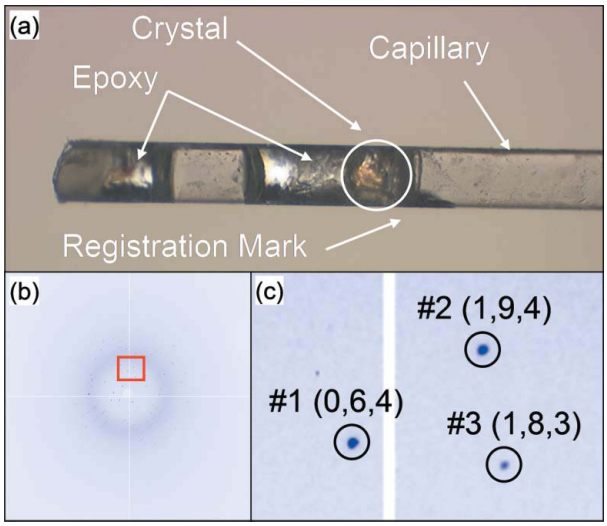

Figure 2
Experimental detail: (*a*) crystal of tetragonal lysozyme (<300 × 300 × 300 µm) mounted inside a capillary with epoxy glue; (*b*) location of the reflections on the ADSC Quantum-4 detector; (*c*) close-up view of the reflections selected for study with the topography camera with reflection number and Miller indices indicated. In (*b*) and (*c*) the crystal rotation axis is horizontal.

the active area of the topography camera. Then a swath of fine-sliced data were collected with the ADSC Quantum-4 detector. This detector was then removed, the topography camera positioned and an identical swath of fine-φ-sliced topography data collected. The crystal was cryocooled in a nitrogen stream. Oscillations followed by stills were taken to determine if the reflections were still in the same region and to determine the angular limits of the selected group of reflections. Fine-sliced topography data were then collected over the predetermined angular range. Finally, the topography camera was stowed and coarse oscillation images followed by fine-φ-sliced data were collected with the ADSC Quantum-4 detector under CR conditions. Details are shown in Table 1.

2.4. Conventional fine-φ-sliced data collection

Prior to the topography experiment, the beamline hardware and software were thoroughly tested and optimized to produce smooth reflection profiles from test crystals. This was necessary because the beamline setup is typically optimized for conventional data collection and the algorithms and motion control parameters created for these experiments are not always appropriate for fine-slicing. Problems with the beamline setup manifest themselves as a jitter in the reflection's intensity when the sequence of images captured to create the reflection profile are animated. The wavelength was set to 0.979 Å and the beam collimated to 0.3 mm diameter for all measurements. A crystal of less than 0.3 mm in each dimension was selected so that the crystal was completely enveloped by the X-ray beam. The crystal to detector distance was 130 mm. Unlike previous fine-slicing work where as many profiles as possible were collected (Bellamy *et al.*, 2000; Borgstahl *et al.*, 2001; Snell *et al.*, 2001), the main interest of this experiment was to obtain the profiles of a selected group of reflections (Fig. 2*c*). Angular ranges for the coarse and fine-sliced measurements were tailored for this approach. Diffraction images were collected with an ADSC Quantum-4 detector using the rotation camera geometry as described elsewhere (Bellamy *et al.*, 2000; Borgstahl *et al.*, 2001). At RT, a sequence of five coarse oscillation images were collected with $\Delta\varphi = 1^\circ$ and an exposure time of 10 s, followed by 700 fine-sliced images that were collected as stills spaced by 0.002° with an exposure time of 1 s. For the cryo-data collection, similar coarse images were collected, followed by 650 fine-sliced images with an exposure time of 2 s (Table 1). All data were collected in constant time mode and not corrected for the change in beam intensity with decaying ring current because the APS was operating in top-up mode and therefore intensity variations during the experiment were negligible.

2.5. Digital topography fine-φ-sliced data collection

To orient the topography camera, the direct beam was recorded by a short exposure with the beamstop removed, but an attenuator in place to minimize damage to the topography detector. The detector was positioned with the x,y positioning system so that the direct beam would be at the center of the detector (pixel location $x = 500$, $y = 500$). The actual x,y positions of the motion system were used to record the topography beam center. The crystal to topography detector distance was approximately 122 mm. Simple geometry was applied to determine the stage positions so that the topography detector would be able to read the selected group of reflections. The final position of the topography detector was verified with the help of oscillation images. Topographs were recorded as stills spaced by 0.002° with 4 s exposures for both CR and RT data (Table 1). Positioning of the topography detector, capturing and preliminary analysis of the topographs was carried out using *Ripple*, an application written specifically for this purpose (Lovelace & Borgstahl, 2006).

2.6. Processing of conventional fine-φ-sliced data

The fine-φ-sliced reflection profiles were analyzed using *BEAM-ish 2.0* (Lovelace & Borgstahl, 2003; Lovelace *et al.*, 2000). For each swath of data, *BEAM-ish* uses *MOSFLM* (Powell, 1999) for processing of the coarse images and obtaining the unit-cell dimensions and the crystal orientation matrix. The space group was $P4_32_12$ with typical tetragonal lysozyme cell dimensions of $a = 79.7$, $b = 79.1$, $c = 37.9$ Å for room temperature, and $a = 78.7$, $b = 78.7$, $c = 36.9$ Å for cryocooled conditions. *MOSFLM* produces a list of all the theoretically observable reflections and their expected positions. All fine-φ-sliced images for that swath are then integrated at the predicted reflection positions and the background is subtracted to obtain the reflection profiles (intensity *versus* φ) (Bellamy *et al.*, 2000). Finally, the resulting profiles were processed to remove 'zingers' (Borgstahl *et al.*, 2001).

2.7. Processing of digital topography fine-φ-sliced data

In the initial step of the image analysis, a reflection topograph was located on the images and a frame of 100×100 pixels was centered over the topograph. Then a stack of frames, each 100×100 pixels wide, was extracted from the raw data. A multi-step process was used to clean-up and correct the data. The steps included subtraction of the dark current, a genetic-algorithm-based correction of a gain imbalance between odd and even pixels, and a wavelet-based resolution enhancement (Lovelace, Soares *et al.*, 2004; Lovelace *et al.*, 2005). This procedure was automated with *Matlab* (The Math Works Inc., 1992). A detailed example of the processing can be found in the supplementary material.[1]

3. Results and discussion

3.1. Sample mounting

Maintaining the crystal orientation during RT data collection and between the transition from RT to CR was necessary in order to collect topography data on an identical set of reflections and to keep all other parameters constant. One of

[1] Supplementary data are available from the IUCr electronic archives (Reference: HE5346). Services for accessing these data are described at the back of the journal.

the biggest challenges was to eliminate crystal motion at RT. Glue was used in the past to fix crystals for diffraction experiments (Knapp *et al.*, 2004; Rayment *et al.*, 1977). Several types of glue were tested and lysozyme crystals seem to be especially resilient in epoxy. General indicators of crystal quality (resolution and mosaicity) were measured by fine-φ-sliced data and indicated that the crystal tolerated the use of glue very well. The crystal was small but diffracted with acceptable resolution (1.90 Å) and at room temperature the reflections had φ_R values of 0.10°. Using a capillary mount we were able to maintain crystal orientation at the two temperatures (Yao *et al.*, 2004). Cryocooling in the capillary also worked very well. An increase in mosaicity was expected after cryocooling and the φ_R values were near 0.40°, which is comparable with the best mosaicities reported for cryocooled lysozyme crystals [0.47° (Sauter *et al.*, 2001) and 0.33° (Lovelace *et al.*, 2005)]. This result indicates that the cryocooling in a capillary with epoxy to immobilize the crystal works similarly to the loop method with glycerol and oil that we had used previously (Lovelace *et al.*, 2005). Scale factors for room-temperature coarse images collected before and after the RT topography run increased by 14%, giving an indication of the level of resilience of lysozyme crystals to radiation damage (Table 1). Therefore, we conclude that the majority of changes seen in the reflection profile upon cryocooling can be associated with the temperature change.

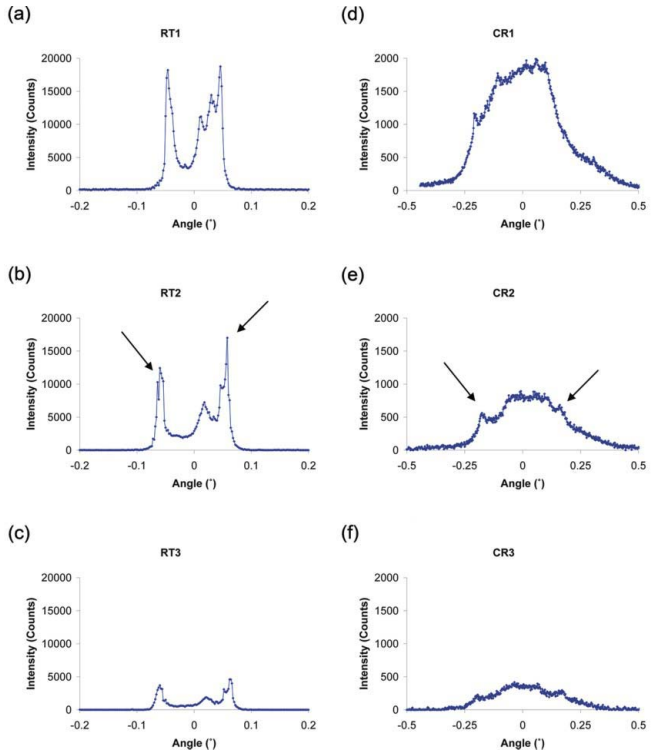

Figure 3
Fine-sliced reflection profiles collected with the ADSC Quantum-4 detector from the three reflections at room temperature, (*a*), (*b*) and (*c*), and after cryocooling (*d*), (*e*) and (*f*).

3.2. Analysis of the reflection profiles

Intensity profiles for the selected group of reflections (Fig. 2*c*) were compiled from the images collected with the Quantum-4 detector at room and cryo temperatures (Fig. 3). Due to the location of the reflections on the detector and the parallel nature of the synchrotron beam, the width of the reflection, φ_R, is nearly the same as the deconvoluted mosaicity η (Bellamy *et al.*, 2000). The φ_R at full width at half-maximum (FWHM) for room-temperature reflections is about 0.1° with peak intensities ranging from 20000 to 5000 counts (Figs. 3*a*–3*c*). When cryocooled, the reflection profiles broadened to 0.4° and peak intensities diminished by a factor of 10. This fourfold increase in width and tenfold decrease in maximum intensity caused by cryocooling is consistent with previously observed results (Vahedi-Faridi *et al.*, 2003). The actual profiles are far more complex than a single Gaussian that an ideal crystal would produce (Fig. 3). Based on the analysis of the peak profile, it appears that this crystal is composed of many mosaic domains, including two large well ordered regions, judged by the intensity spikes at each end of the reflection profile. These prominent peaks disappear upon cryocooling [compare the arrowed positions in Figs. 3(*b*) and 3(*e*)]. Unfortunately, it is not possible to estimate the shape or size of the mosaic domains from the reflection profiles alone.

3.3. Visualization of the three-dimensional topographic data sets

The topographic data consist of a sequence of still images spaced at 0.002° interval. There are many approaches that can be taken to represent these data (Fig. 4). One method would be to create a three-dimensional model of the reflection (Lovelace, Narayan *et al.*, 2004) or the frames could be organized into a movie [the movies (avi format) for all of the reflections are available as supplementary material]. Reorga-

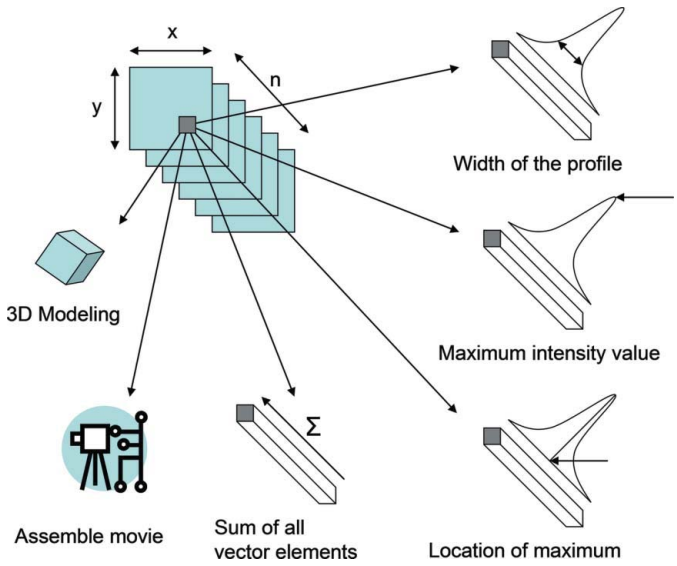

Figure 4
Analysis scheme: stacked images (*x*,*y* arrays) with one *n*-dimensional pixel vector selected. The various analysis methods are indicated (see text for details).

nizing the image sequence into a collection of pixel vectors opens up several other possible representations of the data. Each pixel vector contains the intensities measured for a particular x,y location for the entire image sequence. Operators have been defined that extract information from the pixel vectors. When the result of an operation is a single value, the data set can be represented as a two-dimensional graphic. The first operator that was applied simply returns the sum of the elements in the pixel vector, effectively generating an image that is similar to an oscillation frame with an angular range that encompasses the reflection. A different operator that was defined returned the maximum recorded intensity within the pixel vector. The maximum intensity operator produces an image which indicates areas of enhanced diffraction in the crystal. Another operator that was applied returned the location, *i.e.* pixel element, of the maximum intensity within the pixel vector. This location operator produces a map of the domain structure in the crystal because pixels with a maximum intensity at the same index belong to the same domain. If domains are overlapping (a pixel vector may contain data from multiple domains) then only the one with maximum intensity contribution will be visible in the resulting image. Finally, an operator was defined evaluating each pixel vector as a reflection profile and returning the width (FWHM) of the pixel vector profile φ_R. The result of this operator is an image indicating the homogeneity of the crystal.

Fig. 5 describes the method used to calculate the widths of the reflection profiles. Initially the maximum is located, then a search is conducted for the FWHM locations from the profile extents toward the maximum (Fig. 5, step 2). These two locations are used to calculate the width. If the profile is a simple peak-shaped structure, then the calculated width will be identical to the true FWHM (left side of Fig. 5). If the profile contains multiple peaks, then the estimated width will be too large (right side of Fig. 5). An unusually large width may indicate the intersection of multiple mosaic domain boundaries if neighboring pixel vectors show normal widths, or the region may simply be of very low crystal quality.

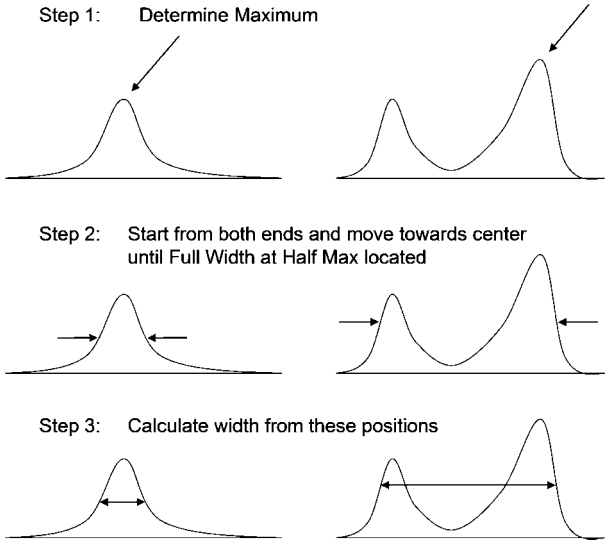

Figure 5
Algorithm used to determine the width of the reflection profile peak contained in topographic data.

3.4. Analysis of the topography data

For the RT reflections, a map of the summation across all pixel vector elements reveals a strongly diffracting region of triangular shape in the upper right of the recorded area (Figs. 6*a*–6*c*). A defect, possibly a grain boundary in the crystal, is highlighted by this analysis (see arrows in Fig. 6), and is most prevalent for the weakest reflection, RT3, where actually a small area shows no diffraction (Fig. 6*c*). When the crystal was

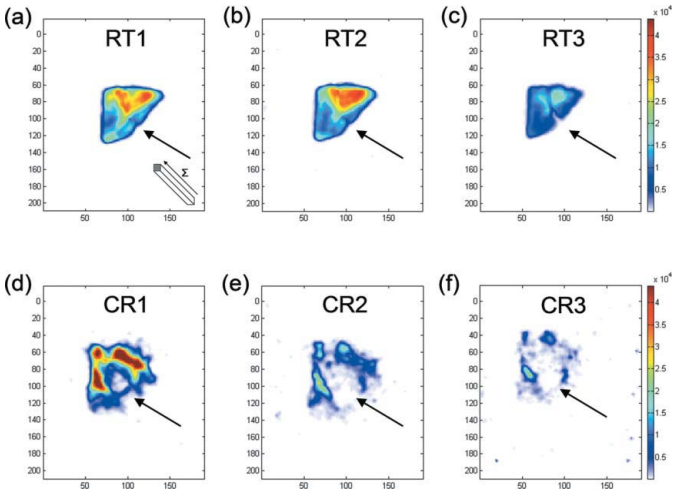

Figure 6
Analysis-of-pixel-vector-sums map. Images (*a*), (*b*) and (*c*) are for room-temperature and images (*d*), (*e*) and (*f*) are for cryocooled reflections. RT# and CR# refers to the temperature; the numbers indicate the reflection identifier from Fig. 2. The circled areas highlight higher background scatter in the CR data. Note: colors indicate integrated intensity counts from low (blue) to high (red).

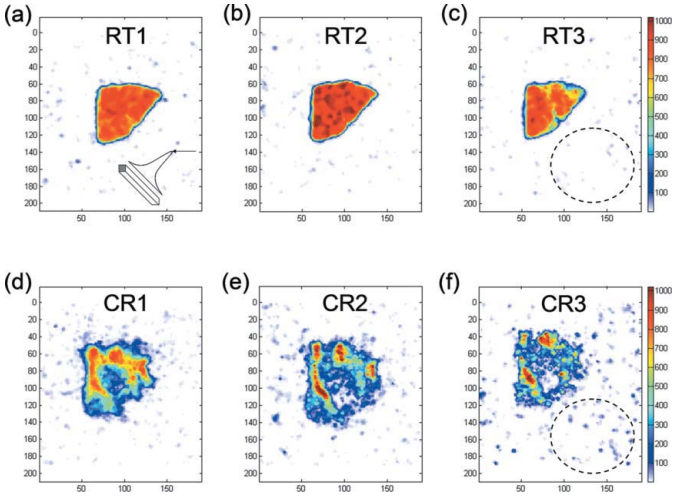

Figure 7
Maximum-intensity-value map. Parts (*a*), (*b*) and (*c*) are for room-temperature and parts (*d*), (*e*) and (*f*) are for cryocooled reflections. Note: colors indicate intensity counts from low (blue) to high (red).

cryocooled, the region near this defect expanded to a diffraction void (Figs. 6*d*–6*f*). The once strong triangular region is no longer recognizable; instead smaller segments of lower intensity loosely arrange around the void. In addition, the CR topographs also indicate a larger cross section for all three reflections (∼1.5-fold) than the RT data. This might be due to the preservation of differential cell sizes as the unit cell contracts on cooling, or due to increased spot size due to increased mosaicity (0.4°) over that distance (130 mm).

Analysis of the data with respect to the maximum intensity value is presented in Fig. 7. The RT data are uniform because during the course of the rocking curve, nearly every segment of the crystal caused saturation of the associated pixel

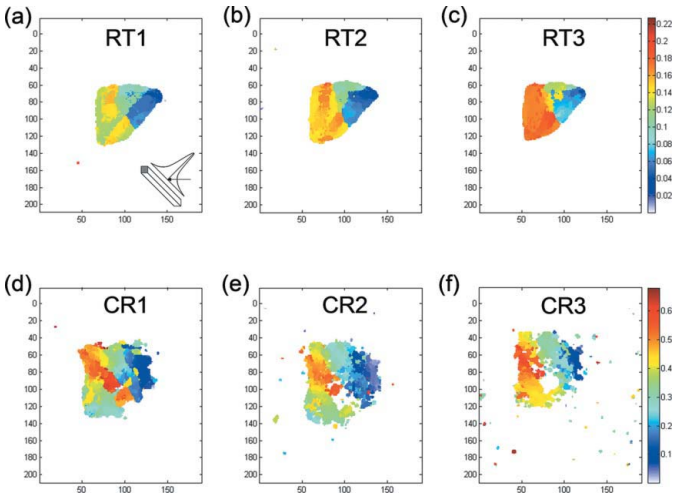

Figure 8
Location-of-maximum map (mosaic-domain map). Parts (*a*), (*b*) and (*c*) are for room-temperature and parts (*d*), (*e*) and (*f*) are for cryocooled reflections. In order to show details in the room-temperature data, the angular (color) scale has been stretched threefold in comparison with the cryocooled color scale to help highlight mosaic domains. Note: colors indicate angular location (°) from the start of the scan (blue) to the end (red).

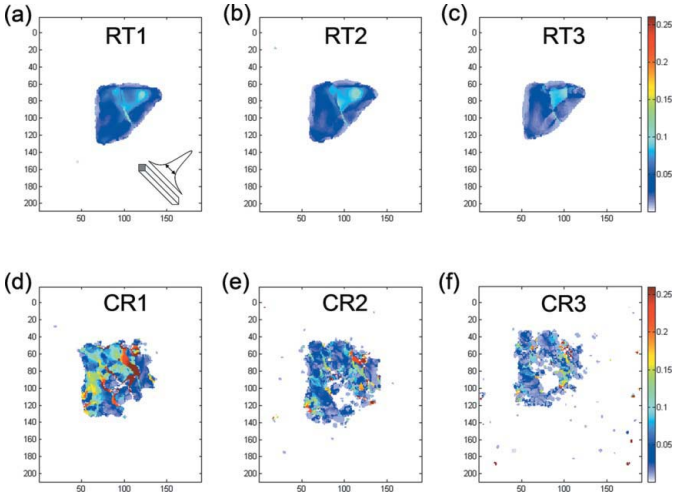

Figure 9
Width-of-the-peak map. Parts (*a*), (*b*) and (*c*) are for room-temperature and parts (*d*), (*e*) and (*f*) are for cryocooled reflections. Note: colors indicate peak width (°) from thin (blue) to thick (red).

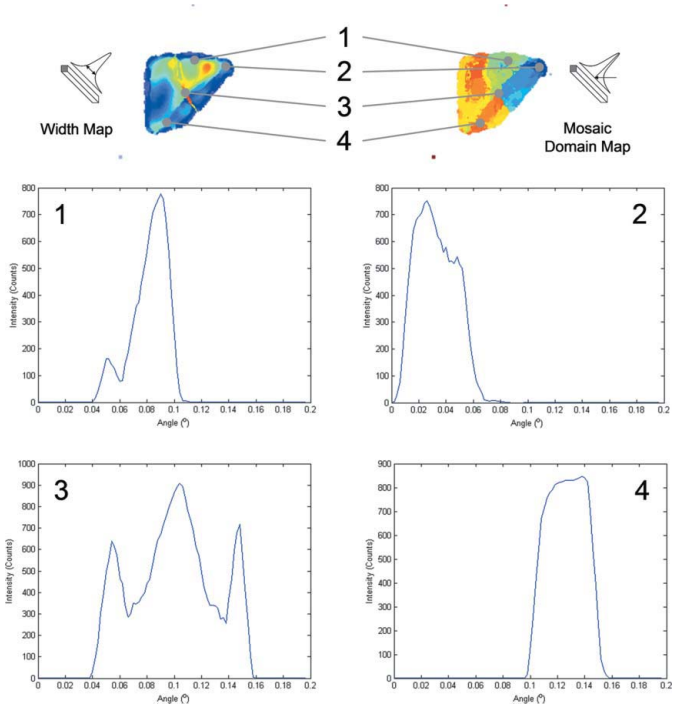

Figure 10
Selected internal room-temperature profiles. Four positions are highlighted on the width-of-the-peak (left) and the location-of-maximum analysis (right) of the RT1 reflection. The associated reflection profiles for these locations are displayed.

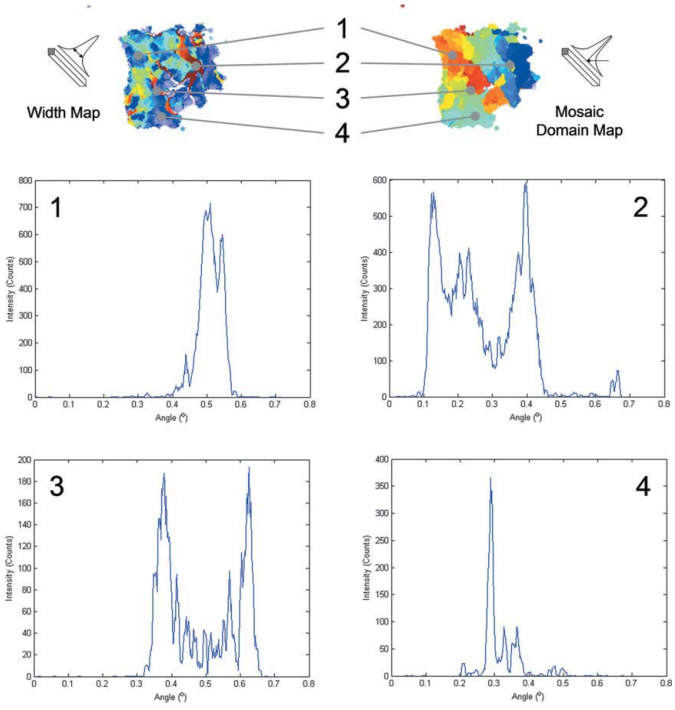

Figure 11
Selected internal cryocooled profiles. Four positions are highlighted on the width-of-the-peak and the location-of-maximum analysis of the CR1 reflection. The associated reflection profiles for these locations are displayed below.

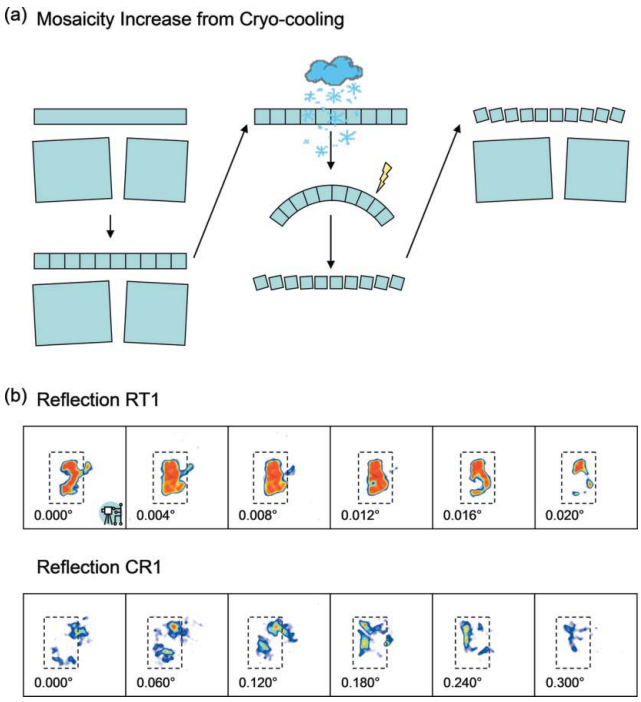

Figure 12
Mosaicity increase from cryocooling. (*a*) Proposed model for increased crystal mosaicity due to cryocooling. (*b*) Supporting topographic sequences for the proposed model, selected from the image stack, explaining increased mosaicity due to cryocooling.

elements of the detector (Figs. 7*a*–7*c*). Note that the camera is equipped with anti-blooming circuitry such that neighboring pixels are not affected if an individual pixel is saturated (Lovelace *et al.*, 2005). Only in the weakest reflection, RT3, some pixels recorded intensities below saturation. For the CR data series, small areas retained maximum diffraction intensity (saturated the detector), but most pixel elements had a maximum value that was far less than for the RT case (Figs. 7*d*–7*f*). In addition, a higher scattering background was recorded (see dashed circles in Figs. 7*c* and 7*f*).

The analysis with respect to the location of maximum intensity reveals three to five major domains within the crystal (Fig. 8). A color scheme is used in Fig. 8 for representation where the maximum intensity was recorded during the data collection, with blue at the beginning and red at the end of the sequence. For the RT conditions, the reflections begin diffracting early in φ (blue) in the upper-right corner and fill in across to the left (yellow) and down to later φ values (red). After cryocooling, the angular relationship between the various domains is generally conserved (*i.e.* similar areas show similar diffraction). However, the angular spread is much larger (compare color scales in Figs. 8*a*–8*c* and Figs. 8*d*–8*f*) and the domain structures are significantly distorted. The sequences of diffraction images (movies are provided as supplementary material) confirm this observation. About half way through the reflection profile, the left-most region of the reflection begins to diffract and moves up. Both regions meet in the upper left-hand side and then there is a small region which fills in from the upper left, down toward the middle.

Analysis of the peak widths shows for the RT data an almost monochrome blue to light-blue color, equivalent to very small widths with little variation across the crystal (Figs. 9*a*–9*c*). These values of $\sim 0.03^\circ$ are smaller than the total reflection profile of 0.1° as determined from the conventional fine-sliced data, but their overall sum is larger than 0.1°, which indicates that the mosaic regions that collectively make up the crystal are overlapping. Under CR conditions, many pixel vectors have surprisingly smaller widths ($\ll 0.1^\circ$) similar to the width observed for the RT case. There are a few areas of larger widths approaching the 0.4° average from the CR fine-slicing data. These areas most likely represent a domain boundary. Combining mosaicity analysis with the mosaic-domain map (Fig. 8) shows that at the pixel vector level the RT and CR mosaic domains have very similar widths, but that they are distributed over a much larger angular range.

Individual pixel vectors taken from four different areas of the topographic sequence were analysed (Figs. 10 and 11). For the RT case, the profiles denoted by regions 1, 2 and 4 indicate, from the width-of-the-peak (left) and the location-of-maximum analysis (right), that these profiles should basically consist of a single peak; however, the profiles seem to be composed of several closely spaced peaks which combine to form a large peak with hints of the underling peak structure (Fig. 10). For profile 3, which is at the intersection of three domains based on the location-of-maximum map, the expected profile should have three major peaks, which was exactly the profile generated from the data. For the CR data, all of the profiles appear to be composed of a large number of very narrow peaks (Fig. 11).

4. Proposed model

This experiment has provided insight into the effects of cooling on the mosaic structure of protein crystals. Based on the observations, we propose the following cooling model, shown in Fig. 12(*a*). A crystal is composed of several (here, three) large mosaic domains (Fig. 12*a*) as seen in Fig. 8. These domains are built from smaller regions that have errors which are too small to be detected with conventional instrumentation. In this example, only one of the domains is followed in depth. During cryocooling, a temperature gradient sweeps across the crystal, creating differential cell sizes as the unit cell contracts during cooling (Snell *et al.*, 2002). This differential contraction causes stress to build up and to become concentrated on the weakest portions of the domain: most likely areas with lattice defects. The stress induced in the crystal does not occur in a random fashion, but follows the temperature gradient. Additional stress arises from the differential solidification of bulk water and solvent in the crystal (Kriminski *et al.*, 2002, 2003). With increasing stress, the sub-domains fracture along their boundaries in an orderly additive fashion (Fig. 9) as the cooling gradient sweeps by, increasing the total number of mosaic domains and macroscopic observed mosaicity.

We believe that this model is directly supported by our topographic experiments and is consistent with previous work

(Kriminski *et al.*, 2002, 2003). In Fig. 12(*b*), a domain is visible at RT as the reflection progresses with angle. The overall domain is highlighted by a dashed box, covering an angular range of only 0.02°. For the CR case, the large domain has fragmented into many smaller domains and the profile is now broadened to 0.3° (Fig. 12*b*). The diffraction profile clearly shows the random orientation of the new elements that make up the original domain. The cryo-introduced fracture is enhanced along the original RT boundaries and leads to the overall angular increase of the reflection. Further experiments will be necessary using different protein crystals and possibly higher-resolution CCD detectors to improve and generalize this model.

5. Conclusions

A particularly significant result is our finding that cryocooling shatters the mosaic structure of the crystal, resulting in a substantial increase in mosaicity but with preservation of the overall RT domain relationships in the cryocooled crystal (compare *e.g.* Figs. 3*b* and 3*e*). Furthermore, we have shown that there is an increased background around the diffraction spots for the cryocooled crystal case (compare *e.g.* Figs. 7*c* and 7*f*). We confirm a dramatic reduction of the reflection peak to background ratio for the increased mosaicity situation, *i.e.* of the cryocooled crystal. This paper highlights the benefits of the steadily improving technologies and techniques for studying protein crystal perfection, which overall seek to improve structure determination capability and possibilities (Helliwell, 2005). The use of colour graphics (Figs. 6–9 and Fig. 12) offers new opportunities to quantify and effectively describe these space–angle maps of reflections visually.

NASA Grant NAG8-1983 supported this work. BioCARS receives support (grant RR07707) from the National Center for Research Resources of the National Institutes of Health. We would like to thank John Helliwell for useful discussions, the staff at BioCARS for their helpful suggestions, flexibility and never-ending patience, and the synchrotron controller who finally deemed our sacrifices worthy and postponed the beam dump until three minutes after our final image was collected.

References

Bellamy, H. D., Snell, E. H., Lovelace, J., Pokross, M. & Borgstahl, G. E. O. (2000). *Acta Cryst.* D**56**, 986–995.
Boggon, T. J., Helliwell, J. R., Judge, R. A., Olczak, A., Siddons, D. P., Snell, E. H. & Stojanoff, V. (2000). *Acta Cryst.* D**56**, 868–880.
Borgstahl, G. E. O., Vahedi-Faridi, A., Lovelace, J., Bellamy, H. D. & Snell, E. H. (2001). *Acta Cryst.* D**57**, 1204–1207.
Colapietro, M., Cappuccio, G., Marciante, C., Pifferi, A., Spagna, R. & Helliwell, J. R. (1992). *J. Appl. Cryst.* **25**, 192–194.
Darwin, C. G. (1922). *Philos. Mag.* **43**, 800–829.
Dobrianov, I., Finkelstein, K. D., Lemay, L. G. & Thorne, R. E. (1998). *Acta Cryst.* D**54**, 922–937.
Fourme, R., Ducruix, A., Riess-Kautt, M. & Capelle, B. (1995). *J. Synchrotron Rad.* **2**, 136–142.
Greenhough, T. J. & Helliwell, J. R. (1982). *J. Appl. Cryst.* **15**, 338–351.
Helliwell, J. R. (2005). *Acta Cryst.* D**61**, 793–798.
Helliwell, J. R. (1988). *J. Cryst. Growth*, **90**, 259–272.
Knapp, J. E., Srajer, V., Pahl, R. & Royer, J. W. E. (2004). *Micron*, **35**, 107–108.
Kriminski, S., Caylor, C. L., Nonato, M. C., Finkelstein, K. D. & Thorne, R. E. (2002). *Acta Cryst.* D**58**, 459–471.
Kriminski, S., Kazmierczak, M. & Thorne, R. E. (2003). *Acta Cryst.* D**59**, 697–708.
Lovelace, J. & Borgstahl, G. E. O. (2003). *J. Appl. Cryst.* **36**, 1101–1102.
Lovelace, J. & Borgstahl, G. E. O. (2006). *J. Appl. Cryst.* **39**, 466–467.
Lovelace, J. J., Murphy, C. R., Bellamy, H. D., Brister, K., Pahl, R. & Borgstahl, G. E. O. (2005). *J. Appl. Cryst.* **38**, 512–519.
Lovelace, J. J., Narayan, K., Chik, J. K., Bellamy, H. D., Snell, E. H., Lindberg, U., Schutt, C. E. & Borgstahl, G. E. O. (2004). *J. Appl. Cryst.* **37**, 327–330.
Lovelace, J., Snell, E. H., Pokross, M., Arvai, A. S., Nielsen, C., Xuong, N.-H., Bellamy, H. D. & Borgstahl, G. E. O. (2000). *J. Appl. Cryst.* **33**, 1187–1188.
Lovelace, J. J., Soares, A. S., Bellamy, H. D., Sweet, R. M., Snell, E. H. & Borgstahl, G. E. O. (2004). *J. Appl. Cryst.* **37**, 481–485.
Lübbert, D., Meents, A. & Weckert, E. (2004). *Acta Cryst.* D**60**, 987–998.
Ludwig, W., Cloetens, P., Härtwig, J., Baruchel, J., Hamelin, B. & Bastie, P. (2001). *J. Appl. Cryst.* **34**, 602–607.
Nave, C. (1998). *Acta Cryst.* D**54**, 848–843.
Otálora, F., García-Ruiz, J. M., Gavira, J. A. & Capelle, B. (1999). *J. Cryst. Growth*, **196**, 546–558.
Powell, H. R. (1999). *Acta Cryst.* D**55**, 1690–1695.
Rayment, I., Johnson, J. E. & Suck, D. (1977). *J. Appl. Cryst.* **10**, 365.
Sauter, C., Otálora, F., Gavira, J.-A., Vidal, O., Giege, R. & Garcia-Ruiz, J. M. (2001). *Acta Cryst.* D**57**, 1119–1126.
Snell, E. H., Judge, R. A., Crawford, L., Forsythe, E. L., Pusey, M. L., Sportiello, M., Todd, P., Bellamy, H., Lovelace, J., Cassanto, J. M. & Borgstahl, G. E. O. (2001). *Cryst. Growth Des.* **1**, 151–158.
Snell, E. H., Judge, R. A., Larson, M. & van der Woerd, M. J. (2002). *J. Synchrotron Rad.* **9**, 361–367.
Snell, E. H., Weisgerber, S., Helliwell, J. R., Weckert, E., Holzer, K. & Schroer, K. (1995). *Acta Cryst.* D**51**, 1099–1102.
Stojanoff, V. & Siddons, D. P. (1996). *Acta Cryst.* A**52**, 498–499.
Stojanoff, V., Siddons, D. P., Monaco, L. A., Vekilov, P. & Rosenberger, F. (1997). *Acta Cryst.* D**53**, 588–595.
Stojanoff, V., Siddons, D. P., Snell, E. H. & Helliwell, J. R. (1996). *Synchrotron Radiat. News*, **9**, 25–26.
The Math Works Inc. (1992). *Matlab Reference Guide*. The Math Works Inc., Natick, MA, USA.
Vahedi-Faridi, A., Lovelace, J., Bellamy, H. D., Snell, E. H. & Borgstahl, G. E. O. (2003). *Acta Cryst.* D**59**, 2169–2182.
Yao, M., Yasutake, Y. & Tanaka, I. (2004). *Acta Cryst.* D**60**, 39–45.